

Dynamical Friction of a Circular-Orbit Perturber in a Gaseous Medium

Hyosun Kim and Woong-Tae Kim

Department of Physics and Astronomy, FPRD, Seoul National University, Seoul 151-742, Korea

hkim@astro.snu.ac.kr, wkim@astro.snu.ac.kr

ABSTRACT

We investigate the gravitational wake due to, and dynamical friction on, a perturber moving on a circular orbit in a uniform gaseous medium using a semi-analytic method. This work is a straightforward extension of Ostriker (1999) who studied the case of a straight-line trajectory. The circular orbit causes the bending of the wake in the background medium along the orbit, forming a long trailing tail. The wake distribution is thus asymmetric, giving rise to the drag forces in both opposite (azimuthal) and lateral (radial) directions to the motion of the perturber, although the latter does not contribute to orbital decay much. For subsonic motion, the density wake with a weak tail is simply a curved version of that in Ostriker and does not exhibit the front-back symmetry. The resulting drag force in the opposite direction is remarkably similar to the finite-time, linear-trajectory counterpart. On the other hand, a supersonic perturber is able to overtake its own wake, possibly multiple times, and develops a very pronounced tail. The supersonic tail surrounds the perturber in a trailing spiral fashion, enhancing the perturbed density at the back as well as far front of the perturber. We provide the fitting formulae for the drag forces as functions of the Mach number, whose azimuthal part is surprisingly in good agreement with the Ostriker's formula, provided $V_p t = 2R_p$, where V_p and R_p are the velocity and orbital radius of the perturber, respectively.

Subject headings: hydrodynamics — galaxies : kinematics and dynamics — ISM: general — shock waves

1. INTRODUCTION

Dynamical friction refers to momentum loss suffered by a massive object moving through a background medium due to its gravitational interaction with its own induced wake. The

gravitational drag force removes angular momentum from an object in orbital motion, causing it to gradually spiral in toward the center of the orbit. In a pioneering study, Chandrasekhar (1943) derived the classical formula of dynamical friction in a uniform collisionless background, the result of which has been applied to a number of astronomical systems. Examples include orbital decay of satellite galaxies orbiting their host galaxies (e.g., Tremaine 1976; Lin & Tremaine 1983; Weinberg 1989; Hashimoto et al. 2003; Fujii et al. 2006; see also Binney & Tremaine 1987), dynamical fates of globular clusters near the Galactic center (e.g., Kim & Morris 2003; McMillan & Portegies Zwart 2003; Kim et al. 2004), galaxy formation within the framework of hierarchical clustering scenario (e.g., Zentner & Bullock 2003; Bullock & Johnston 2005 and references therein), formation of Kuiper-belt binaries (Goldreich et al. 2002), and planet migrations (Del Popolo et al. 2003) via interactions with planetesimals, etc.

Although less well recognized, dynamical friction also operates in gaseous backgrounds. Using a time-dependent linear perturbation theory, Ostriker (1999, hereafter O99) derived the analytic expressions for the density wake and drag force for a perturber in a uniform gaseous medium. O99 showed that resonant interactions between a perturber and pressure waves make the gaseous drag more efficient than the collisionless drag when the Mach number $\mathcal{M} \sim 1$. She also found that even a subsonic perturber experiences a nonvanishing gaseous drag if interaction time between the perturber and the background is finite. This is an improvement on the previous notion that the gaseous drag is absent for subsonic perturbers because of the front-back symmetry in the steady-state density wake (Dokuchaev 1964; Ruderman & Spiegel 1971; Rephaeli & Salpeter 1980).

The results of O99 were confirmed numerically by Sánchez-Salcedo & Brandenburg (1999) and have been applied to various situations including massive black hole mergers in galactic nuclei (e.g., Escala et al. 2004; Liu 2004; Escala et al. 2005; Dotti et al. 2006), orbital decay of compact objects (e.g., Narayan 2000; Karas & Šubr 2001) and associated viscous heating (e.g., Chang 2001; Chang & Choi 2003) in accretion disks, and heating of an intracluster medium by supersonically moving galaxies in clusters (e.g., El-Zant et al. 2004; Faltenbacher et al. 2005; Kim et al. 2005). Without involving shocks, density wakes in a collisionless medium are distributed more smoothly and achieve larger amplitudes than those in a gaseous medium (Mulder 1983), which led Furlanetto & Loeb (2002) to suggest that X-ray emissions from galaxy wakes can in principle be used to discern the collisional character of dark matter in galaxy clusters.

While the results of Chandrasekhar (1943) and O99 are simple and provide good physical insights, they apply strictly to a mass traveling on a straight-line trajectory through an infinite homogeneous background. Real astronomical systems obviously have nonuniform

density distributions and perturbers tend to follow curvilinear orbits. For instance, motions of galaxies in galaxy clusters, binary black holes near the central parts of galaxies, and compact stars in accretion disks are better approximated by near-circular than straight-line orbits, and their background media usually in hydrostatic equilibrium are stratified in the radial direction. Even for objects experiencing orbital decay, a near-circular orbit is a good approximation if the associated friction time is longer than the orbital time. Consideration of a circular-orbit perturber is of particular interest since it will allow the perturber, if supersonic, to overtake the backside of its wake that was created about an orbital period earlier. In this case, a steady-state wake that eventually forms has morphology and drag force that might be significantly different from the linear-trajectory counterparts. Numerical simulations carried out by Sánchez-Salcedo & Brandenburg (2001) and Escala et al. (2004) indeed show that the density wake by a near-circular orbit perturber contains a trailing spiral tail, which is absent in the linear-trajectory cases. They also showed that the resulting drag force is smaller than the estimate based on the formula given in O99, which is probably due to the near-circular orbit, although the effect of nonuniform backgrounds in their models cannot be ignored completely.

The drag formula based on perturbers moving straight in either a collisionless medium or a gaseous medium depends on the Coulomb logarithm $\ln(\Lambda) \equiv \ln(r_{\max}/r_{\min})$, where r_{\min} and r_{\max} are the cutoff radii introduced to avoid a divergence of the force integrals.¹ While many previous studies conventionally adopted r_{\min} and r_{\max} as the characteristic sizes of the perturber and the background medium, respectively, the choice of r_{\max} remains somewhat ambiguous for objects moving on near-circular orbits (e.g., Binney & Tremaine 1987). For *collisionless* backgrounds, Hashimoto et al. (2003) and Fujii et al. (2006) performed N-body experiments for orbital evolution of satellite galaxies in a spherical halo, and found that the Coulomb logarithm with r_{\max} varying proportionally to the orbital radius rather than fixed to the system size gives better fits to their numerical results (see also Tremaine 1976). We shall show in the present work that a similar modification of the Coulomb logarithm is necessary in order to apply the results of O99 to perturbers on near-circular orbits in *gaseous* backgrounds, as well.

In this paper, we consider a perturber moving on a circular orbit in a uniform gaseous medium. Using a linear semi-analytic approach, we explore the structure of the density wake, evaluate the drag force on the perturber, and compare them with those in the straight-line trajectory cases. In §2, we revisit the linear perturbation analysis of O99 for the perturbed density response and apply it to the case of a circular-orbit perturber. We solve the resulting

¹For a perturber moving with velocity V_p through a gaseous medium, $r_{\max} = V_p t$, where t denotes time elapsed since the perturber was introduced (O99).

equations numerically. In §3, we present the numerical results for the wakes and drag forces with varying Mach number. We provide simple fitting expressions to the numerical results, and show that Ostriker’s formula still gives a good estimate for the drag force on a circular-orbit perturber only if the outer cutoff radius in the Coulomb logarithm is taken equal to the orbital diameter of the perturber. In §4, we summarize the present work and briefly discuss our finding.

2. FORMULATION

2.1. Formal Solution for Density Wake

We consider the response of gas to a point-mass perturber moving on a circular orbit and calculate the resulting gravitational drag force on the perturber. We treat the gas as an inviscid, adiabatic fluid, and do not consider the effects of magnetic fields as well as gaseous self-gravity. The governing equations for ideal hydrodynamics are

$$\frac{\partial \rho}{\partial t} + \nabla \cdot (\rho \mathbf{v}) = 0, \quad (1)$$

and

$$\frac{\partial \mathbf{v}}{\partial t} + \mathbf{v} \cdot \nabla \mathbf{v} = -\frac{1}{\rho} \nabla P - \nabla \Phi_{\text{ext}}, \quad (2)$$

where Φ_{ext} is the gravitational potential of the perturber. Other symbols have their usual meanings.

Following O99, we consider an initially uniform gaseous medium with density ρ_0 . Assuming that the wake induced by the perturber remains at small amplitudes, we linearize equations (1) and (2) using $\rho = \rho_0[1 + \alpha(\mathbf{x}, t)]$ and $\mathbf{v} = c_s \boldsymbol{\beta}(\mathbf{x}, t)$, where c_s is the adiabatic speed of sound in the unperturbed medium and α and $\boldsymbol{\beta}$ denote the dimensionless density and velocity perturbations, respectively. Eliminating $\boldsymbol{\beta}$ from the linearized equations, one obtains a three-dimensional wave equation

$$\nabla^2 \alpha - \frac{1}{c_s^2} \frac{\partial^2 \alpha}{\partial t^2} = -\frac{4\pi G}{c_s^2} \rho_{\text{ext}}(\mathbf{x}, t), \quad (3)$$

where $\rho_{\text{ext}} = \nabla^2 \Phi_{\text{ext}} / (4\pi G)$ represents the mass density of the perturber. The formal solution to equation (3) based on the retarded Green function technique is given by

$$\alpha(\mathbf{x}, t) = \frac{G}{c_s^2} \iint d^3 x' dt' \rho_{\text{ext}}(\mathbf{x}', t') \frac{\delta[t' - (t - |\mathbf{x} - \mathbf{x}'|/c_s)]}{|\mathbf{x} - \mathbf{x}'|} \quad (4)$$

(O99; see also Jackson 1975). In the case of a perturber on a straight-line trajectory, O99 solved equation (4) directly to obtain an expression for the perturbed density. The same result was found by Furlanetto & Loeb (2002) who independently used a Fourier transform method in both space and time variables.

2.2. Density Wake for Circular-Orbit Perturbers

We now concentrate on the case where a point-mass perturber with mass M_p moves on a circular orbit with a fixed orbital radius R_p and a constant velocity V_p in an otherwise uniform gaseous medium; the angular speed of the perturber is $\Omega = V_p/R_p$. It is convenient to work in cylindrical coordinates (R, φ, z) whose origin lies at the center of the orbit. The \hat{z} -axis points perpendicular to the orbital plane. Assuming that the perturber is introduced at $(R_p, 0, 0)$ when $t = 0$, one can write $\rho_{\text{ext}}(\mathbf{x}, t) = M_p \delta(R - R_p) \delta[R_p(\varphi - \Omega t)] \delta(z) \mathcal{H}(t)$, where $\mathcal{H}(t)$ is a Heaviside step function. Equation (4) is then reduced to

$$\alpha(\mathbf{x}, t) = \frac{GM_p}{c_s^2 R_p} \int dw \frac{\delta\left(w + s + \mathcal{M} d(w; \tilde{R}, \tilde{z})\right)}{d(w; \tilde{R}, \tilde{z})} \mathcal{H}\left(\frac{w + \varphi}{\Omega}\right), \quad (5)$$

where $w \equiv \varphi' - \varphi$ and $s \equiv \varphi - \Omega t$ are angular distances in the $z = 0$ plane²,

$$d(w; \tilde{R}, \tilde{z}) \equiv \frac{|\mathbf{x} - \mathbf{x}'|}{R_p} = \left(1 + \tilde{R}^2 + \tilde{z}^2 - 2\tilde{R} \cos w\right)^{1/2}, \quad (6)$$

and $\mathcal{M} \equiv V_p/c_s$ is the Mach number of the perturber. In equation (6), $\tilde{R} \equiv R/R_p$ and $\tilde{z} \equiv z/R_p$.

Figure 1 schematically illustrates the situation at the orbital plane and the meanings of variables used in equation (5). At time t , the perturber is located at $\mathbf{x}_p = (R_p, \Omega t, 0)$. During its journey along the thick curve, the perturber continuously launches sound waves that propagate into the background gaseous medium. The position $\mathbf{x} = (R, \varphi, z)$ denotes a region of interest in the surrounding gas where the density response will be evaluated. Since the sound waves have finite traveling time, only the signals emitted by the perturber at the location(s) $\mathbf{x}' = (R_p, \varphi', 0)$ at the retarded time $t' = t - |\mathbf{x} - \mathbf{x}'|/c_s$ are able to affect the point \mathbf{x} at time t . Note that s and w represent the projected angular distances in the orbital plane between \mathbf{x}_p and \mathbf{x} and between \mathbf{x}' and \mathbf{x} , respectively. The symbol d in equation (6) refers to the three-dimensional linear distance between \mathbf{x}' and \mathbf{x} normalized by R_p .

²Note that w and s in O99 are defined as *linear* distances along the line of motion, while they measure *angular* distances in the present work.

Using the identity $\delta[f(w)] = \sum_i \delta(w-w_i)/|f'(w_i)|$, where w_i are the roots of an arbitrary function $f(w)$, equation (5) is further simplified to

$$\alpha(\mathbf{x}, t) = \frac{GM_p}{c_s^2 R_p} \mathcal{D}(\mathbf{x}, t), \quad (7)$$

with the dimensionless perturbed density

$$\mathcal{D}(\mathbf{x}, t) = \sum_{w_i} \frac{\mathcal{M}}{|w_i + s - \mathcal{M}^2 \tilde{R} \sin w_i|} \mathcal{H}\left(\frac{w_i + \varphi}{\Omega}\right). \quad (8)$$

Here, the summation is over all possible roots w_i that satisfy the condition

$$\mathcal{M} d(w_i; \tilde{R}, \tilde{z}) = -(w_i + s), \quad (9)$$

for fixed values of \tilde{R} , \tilde{z} , and s . The function $\mathcal{H}[(w_i + \varphi)/\Omega]$ in equation (8) defines the region of influence (or casual region) outside of which sonic perturbations sent off by the perturber at $t = 0$ have insufficient time to reach. For $\tilde{R}, \tilde{z}, \Omega t \gg 1$, equation (9) yields $w_i + \varphi = \Omega t - \mathcal{M}(\tilde{R}^2 + \tilde{z}^2)^{1/2}$, so that the region of influence corresponds roughly to a sphere with radius $c_s t$ centered at the orbital center. Appendix A presents limiting solutions of equation (8) near the perturber.

Since d is a periodic function of w with period 2π , equation (9) has at least one real root and may possess multiple roots for w_i depending on the values of \mathcal{M} , \tilde{R} , \tilde{z} , and s . In Appendix B, we describe how the number of solutions of equation (9) vary with the Mach number of a perturber. It turns out that there is only a single root for w_i everywhere for a subsonic, circular-orbit perturber, which is the same as in the straight-line trajectory case (O99). When a circular-orbit perturber moves at a supersonic speed, however, equation (9) has an odd number of roots that contribute to the wake in a steady state, which is distinct from the straight-line trajectory case where only one or two points along the orbit influence the wake.

2.3. Gravitational Drag Force

Once the gravitational wake $\alpha(\mathbf{x}, t)$ is found, it is straightforward to evaluate the drag force exerted on the perturber:

$$\mathbf{F}_{\text{DF}} = GM_p \rho_0 \int d^3 \mathbf{x} \frac{\alpha(\mathbf{x}, t) (\mathbf{x} - \mathbf{x}_p)}{|\mathbf{x} - \mathbf{x}_p|^3}. \quad (10)$$

In the straight-line trajectory case studied by O99, $\alpha(\mathbf{x}, t)$ always remains cylindrically symmetric with respect to the line of motion, resulting in the drag force in the anti-parallel

direction. When the perturber is on a circular orbit, $\alpha(\mathbf{x}, t)$ loses the cylindrical symmetry and instead becomes symmetric relative to the orbital plane, making the vertical component of \mathbf{F}_{DF} vanish.

We decompose the nonvanishing parts into the radial and azimuthal components:

$$\mathbf{F}_{\text{DF}} = -\mathcal{F} (\mathcal{I}_R \hat{\mathbf{R}} + \mathcal{I}_\varphi \hat{\boldsymbol{\varphi}}), \quad \mathcal{F} \equiv \frac{4\pi\rho_0(GM_p)^2}{V_p^2} \quad (11)$$

where

$$\mathcal{I}_R = -\frac{\mathcal{M}^2}{4\pi} \int d^3\tilde{\mathbf{x}} \frac{\mathcal{D}(\mathbf{x}, t) (\tilde{R} \cos s - 1)}{(1 + \tilde{z}^2 + \tilde{R}^2 - 2\tilde{R} \cos s)^{3/2}}, \quad (12a)$$

and

$$\mathcal{I}_\varphi = -\frac{\mathcal{M}^2}{4\pi} \int d^3\tilde{\mathbf{x}} \frac{\mathcal{D}(\mathbf{x}, t) \tilde{R} \sin s}{(1 + \tilde{z}^2 + \tilde{R}^2 - 2\tilde{R} \cos s)^{3/2}}. \quad (12b)$$

Note that \mathcal{I}_R measures the drag force along the lateral direction of the instantaneous perturber motion, while \mathcal{I}_φ is for the backward direction. The dimensional term \mathcal{F} in equation (11) allows to directly compare \mathcal{I}_R and \mathcal{I}_φ with the linear-trajectory counterparts (see eq. [12] of O99). As we shall show in §4, it is the azimuthal drag \mathcal{I}_φ that is responsible for the orbital decay of a perturber.

2.4. Numerical Method

We solve equations (8) and (9) numerically to find the perturbed density distribution $\mathcal{D}(\mathbf{x}, t)$ for given \mathcal{M} and t . We first construct a three-dimensional Cartesian mesh centered at the center of the orbit, and solve equation (9) for w_i at each grid point using a hybrid Newton-bisection method. By checking the conditions for multiple roots discussed in Appendix B, we ensure that we do not miss any solution for w_i . The corresponding drag forces \mathcal{I}_R and \mathcal{I}_φ are calculated by direct integration of equations (12).

Since the density wake often exhibits sharp discontinuities especially for supersonic perturbers and is distributed over a large spatial range, it is important to check that the drag forces we calculate do not depend on the size of the computational box and its resolution. For fixed \mathcal{M} , we repeated the calculations with varying box size and resolution and found that depending on the Mach number, the box size of $\sim (20-100)R_p$ and resolution of $\sim (80-640)$ grids per $1R_p$ are sufficient to guarantee good convergence of the drag forces. Although the density perturbations are non-zero outside the box, they have very low amplitudes and are located far from the perturber, providing a negligible contribution to the drag. Very high resolution calculations are required for Mach numbers near the critical values \mathcal{M}_n , in which cases the wake tails become thin and dense (see Appendix B).

3. RESULTS

3.1. Density Wake

3.1.1. Supersonic Cases

We begin by illustrating temporal evolution of density perturbations induced by a supersonic perturber. Figure 2 shows snapshots of the density wake and the corresponding number of roots of equation (9) at the orbital plane for $\mathcal{M} = 2.0$. Time is expressed in units of R_p/c_s . The black circle represents the orbit of a perturber which, introduced at $(R, \varphi, z) = (R_p, 0, 0)$ initially, moves in the counterclockwise direction. At early time ($t \lesssim 1.5$), the density wake consists of a Mach cone and a sonic sphere that are curved along the orbit. Except the bending, the overall wake structure, not to mention the number of solutions for w_i which is either one or two inside the casual region, is the same as in the straight-line trajectory case of O99. As the wake bends further, the Mach cone and the sonic sphere become folded at the innermost interface, creating high-density regions near the center ($t = 1.8$). The wake expands with time at a sonic speed and the Mach cone becomes elongated further.

Unlike in the case of a straight-line trajectory where the Mach cone and the sonic sphere never interact with each other, the perturber (and the head of the Mach cone) on a circular orbit is able to enter its own wake, providing additional perturbations for some regions inside the sonic sphere. Alternatively, this can be viewed as the sonic sphere whose center lies at the initial position of the perturber expands radially outward, swallowing a part of the elongated Mach cone. Consequently, the overlapping of the Mach cone and the sonic sphere creates a high-density trailing tail that has received perturbations three times from the perturber ($t \gtrsim 1.9$). Figure 2 shows that immediate outside the sonic sphere, there still exists a region of the undisturbed Mach cone with two w_i 's. As time proceeds, however, this region moves away from the perturber and thus gives an increasingly small contribution to the drag force. In a steady state which is attained at $t \rightarrow \infty$, the entire domain is affected either once or three times by the perturber.

Figure 3 displays the steady-state distributions of the density wake for $\mathcal{M} = 2.0$ on the $x/R_p = 1$, $y = 0$, and $z = 0$ planes, which clearly shows that the trailing tail loosely wraps around the perturber. The tail becomes narrower with increasing $|z|$. A close inspection of the tail at the $z = 0$ plane shows that density becomes smaller away from the perturber along the tail and is largest at the edges across the tail. This is similar to the density distribution inside the Mach cone in the linear trajectory case where diverging flows (and reduced gravitational potential) after the shock cause density to decrease away from the shock front (and the perturber). This suggests that the edges of the tail are shock fronts.

The outer edge of the tail shown in Figure 3 that connects smoothly all the way to the perturber corresponds indeed to the surface of the curved Mach cone (see also Fig. 1). On the other hand, the inner edge of the tail traces the interface between the Mach cone and the sonic sphere that is newly swept up by the expanding sonic sphere (see Fig. 2). Appendix C proves that the half-opening angle of the head of the curved Mach cone in the $z = 0$ plane is equal to $\sin^{-1}(1/\mathcal{M})$, entirely consistent with the case of a linear trajectory.

The wake tail becomes thicker as \mathcal{M} increases from unity. Figure 4 shows the steady-state density wakes as well as the number of w_i 's that contribute to \mathcal{D} for $\mathcal{M} = 4.0$ and $\mathcal{M} = 5.0$ at the $z = 0$ plane. In both panels, the perturber moving in the counterclockwise direction is located at $x/R_p = 1, y = 0$. When $\mathcal{M} = 4.0$, the tail is fat enough to cover most of the space except near the center and a narrow lane between the tail edges. At $\mathcal{M}_1 \approx 4.603$, the inner edge of the tail eventually touches the neighboring outer edge, enabling three w_i for the entire region under the conditions expressed by equation (B1). When the Mach number is slightly larger than \mathcal{M}_1 , the tail overlaps itself. This in turn creates a new tail with five w_i 's, as Figure 4b displays. As \mathcal{M} increases further, the new tail again becomes thicker, starts to overlap at $\mathcal{M}_2 \approx 7.790$, and produces a narrow lane with seven w_i 's when $\mathcal{M} > \mathcal{M}_2$. The same pattern repeats with increasing \mathcal{M} , and equation (B3) determines the critical Mach numbers.

3.1.2. Subsonic Cases

Unlike in the supersonic cases where a perturber can overtake its own wake and create a tail with complicated structure, sonic perturbations generated by a subsonic perturber produce a gravitational wake that is spatially smooth and does not involve a shock. Since perturbations propagate faster than a perturber with $\mathcal{M} < 1$, the whole casual region is affected by a perturber just once, corresponding to a single w_i at any position. Figure 5 shows the slices of the perturbed density for $\mathcal{M} = 0.5$ in the $x/R_p = 1, y = 0$, and $z = 0$ planes when a steady state is reached. Again, the perturber is located at $x/R_p = 1, y = z = 0$. The density structure in the $z = 0$ plane is simply a curved version of what a linear-trajectory perturber would produce. In particular, as Appendix A shows, the iso-density surfaces near the perturber have the shapes of oblate spheroids with ellipticity $e = \mathcal{M}$, with the short axis parallel to the direction of the motion of the perturber, a characteristic feature of a subsonic wake created by a linear-trajectory perturber (O99).

Notice, however, that the bending of wakes in circular-orbit cases makes the perturbed density distributions intrinsically asymmetric. This results in nonvanishing drag forces even in a steady state, and the dominant contribution to the drag comes from high-density regions

near the perturber. This is markedly different from the purely steady-state linear-trajectory cases where a subsonic perturber experiences no drag due to the front-back symmetry of a wake about the perturber (e.g., Rephaeli & Salpeter 1980). Even if the finite interaction time between the straight-line perturber and the background gas is considered, regions with symmetric perturbed density close to the perturber exert zero net force (O99). Nevertheless, the resulting drag force in the backward direction of motion on a circular-orbit perturber is almost the same as that in the linear-trajectory cases, as we will show in the next subsection. Compared with supersonic cases, the tail in a subsonic wake is short, loosely wound, and very weak, suggesting that its contribution to the drag force is negligible.

3.2. Gravitational Drag Force

As sonic perturbations launched from a perturber at $t = 0$ propagate radially outward, the volume of space exerting the gravitational drag on the perturber grows with time. Figure 6 plots the drag force as functions of time for a few chosen Mach numbers. The solid and dotted lines are for \mathcal{I}_φ and \mathcal{I}_R , respectively. Since $\mathcal{D}(\mathbf{x}, t)$ is singular at $\mathbf{x} = \mathbf{x}_p$, only the region with $r > r_{\min} = R_p/10$ is taken into account in force computation, where r is the three-dimensional distance measured from the perturber; the dependence on r_{\min} will be checked below. The drag force on a subsonic perturber increases almost linearly with time before turning abruptly to a constant value, whereas a supersonic wake with a high-density tail gives rise to slow fluctuations in the drag at early time. At any event, both components of the drag force converge to respective steady-state values, typically within the sound crossing time over the distance equal to the orbital diameter or within about an orbital period when \mathcal{M} is of order unity. The primary reason for this is of course because the perturbed density decreases quite rapidly with r and also because gravity is an inverse-square force. This is unlike the case of a straight-line trajectory where the drag increases secularly as $\ln(V_p t)$ for $\mathcal{M} > 1$. The fast convergence of the drag force guarantees that one can use the steady-state values of \mathcal{I}_φ and \mathcal{I}_R for all practical purposes.

Next, we check the dependence of the drag force on $r_{\min} (\ll R_p)$. Figure 7 shows the results for $\mathcal{M} = 0.5, 2.0,$ and 4.0 . The sizes of errorbars associated with finite grid resolution are smaller than the radius of a solid circle at each data point. First of all, the drag force, \mathcal{I}_R , in the radial direction converges to a constant value as r_{\min} decreases for both subsonic and supersonic cases. On the other hand, the drag force, \mathcal{I}_φ , in the opposite direction of the orbital motion, varies as $\ln(1/r_{\min})$ with decreasing r_{\min} for supersonic perturbers, while independent of r_{\min} for subsonic perturbers. This dependence of \mathcal{I}_φ on small r_{\min} for circular-orbit perturbers is exactly the same as in the linear trajectory cases, which makes

sense because the curvature of a circular orbit is almost negligible in a tiny volume near the perturber.

We plot in Figure 8 the steady-state drag forces for a circular-orbit perturber as functions of the Mach number. For all the points, $r_{\min} = R_p/10$ is taken and numerical convergence is checked. Filled circles give $\mathcal{I}_\varphi/\mathcal{M}^2$, while open circles are for $\mathcal{I}_R/\mathcal{M}^2$, which can be compared with Figure 3 of O99. For practical use, we fit the data using

$$\mathcal{I}_R = \begin{cases} \mathcal{M}^2 10^{3.51\mathcal{M}-4.22}, & \text{for } \mathcal{M} < 1.1, \\ 0.5 \ln [9.33\mathcal{M}^2(\mathcal{M}^2 - 0.95)], & \text{for } 1.1 \leq \mathcal{M} < 4.4, \\ 0.3 \mathcal{M}^2, & \text{for } 4.4 \leq \mathcal{M}, \end{cases} \quad (13)$$

and

$$\mathcal{I}_\varphi = \begin{cases} 0.7706 \ln \left(\frac{1+\mathcal{M}}{1.0004-0.9185\mathcal{M}} \right) - 1.4703\mathcal{M}, & \text{for } \mathcal{M} < 1.0, \\ \ln [330(R_p/r_{\min})(\mathcal{M} - 0.71)^{5.72}\mathcal{M}^{-9.58}], & \text{for } 1.0 \leq \mathcal{M} < 4.4, \\ \ln [(R_p/r_{\min})/(0.11\mathcal{M} + 1.65)], & \text{for } 4.4 \leq \mathcal{M}, \end{cases} \quad (14)$$

which are drawn as solid lines in Figure 8. The fits are within 4% of our semi-analytic results for $\mathcal{M} < 4.4$ and within 16% for $\mathcal{M} > 4.4$. Both components of the drag force peak at $\mathcal{M} \sim 1.2 - 1.4$, analogous to the linear-trajectory cases, and \mathcal{I}_φ dominates over \mathcal{I}_R for transonic perturbers. Although \mathcal{I}_R is larger than \mathcal{I}_φ for $\mathcal{M} \gtrsim 2.2$, its effect on orbital decay of a perturber is insignificant (see §4). The local bumps in the drag forces at $\mathcal{M} \approx 4.6$ and 7.8 are due to the self-overlapping of a wake tail explained in §3.1.1.

Figure 8 also plots as dotted curves the results of O99 for drag force on linear-trajectory perturbers. Despite the difference in the shape of the orbits, the agreement between \mathcal{I}_φ and Ostriker’s formula is excellent for the subsonic case. This presumably reflects the fact that other than bending, the wake structure created by a subsonic circular-orbit perturber is not significantly different from the linear-trajectory counterpart (see §3.1.2). Note also that Ostriker’s formula for the supersonic case, for which $V_p t = 2R_p$ is adopted to fit our numerical results, is overall in good agreement with \mathcal{I}_φ for a range of \mathcal{M} . It is remarkable that the subsonic and supersonic drag formulae (with $V_p t$ chosen adequately in supersonic cases) obtained from perturbers moving straight still give a reasonably good estimate for the drag even on circular-orbit perturbers.

4. SUMMARY AND DISCUSSION

We have taken a semi-analytic approach to study the gravitational wake and the associated drag force on a perturber moving on a circular orbit in an infinite, uniform gaseous

medium. This work extends Ostriker (1999) who studied the cases with straight-line trajectory perturbers. The circular orbit generally causes the wake to bend along the orbit and creates a trailing tail. For a subsonic perturber, the density wake has a weak tail and is distributed quite smoothly (see Fig. 5). On the other hand, a supersonic perturber can catch up with its own wake, possibly multiple times depending on the Mach number, forming a very pronounced trailing tail across which density changes abruptly (see Fig. 3). Although the region influenced by the perturber keeps expanding with time into the surrounding medium, the drag force promptly saturates to a steady state value within less than the crossing time of sound waves over the distance equal to the orbital diameter.

Because of asymmetry in the density wake, it is desirable to decompose the drag force into two components: \mathcal{I}_R and \mathcal{I}_φ in the radial and azimuthal directions, respectively (eq. [11]). Figure 8 plots our main results for \mathcal{I}_R and \mathcal{I}_φ as functions of the Mach number \mathcal{M} ; equations (13) and (14) give the algebraic fits to the numerical results. The azimuthal drag force varying rather steeply with \mathcal{M} peaks at $\mathcal{M} \sim 1.2 - 1.4$, while the radial force is highly suppressed at $\mathcal{M} < 1$ and exceeds the azimuthal drag at $\mathcal{M} \gtrsim 2.2$. It is remarkable that the drag on linear-trajectory perturbers given in O99 is almost identical to \mathcal{I}_φ for subsonic cases, and gives a good approximation for supersonic cases, too, provided $V_p t = 2R_p$.

A striking feature in gravitational wakes formed by circular-orbit perturbers is a long tail in a trailing spiral shape. Such a tail structure is indeed commonly seen in recent hydrodynamic simulations for black hole mergers in a gaseous medium (e.g., Escala et al. 2004, 2005; Dotti et al. 2006; see also Sánchez-Salcedo & Brandenburg 2001). Albeit much weaker, it is also apparent in N-body simulations for satellite orbital decay in a collisionless background (e.g., Weinberg 1989; Hernquist & Weinberg 1989). For supersonic perturbers, the tail is a curved Mach cone and bounded by the shock fronts that propagate radially outward. As explained in Appendices B and C, the outer edge of the tail is described by $\Omega t - \varphi = w_+ + y_+$, where w_+ and y_+ are defined through equation (B2). By taking a time derivative of this equation for fixed φ , one can show that the propagation speed \dot{R}_{sh} of the spiral tail in the radial direction is given by $\dot{R}_{\text{sh}}/c_s = \mathcal{M}\tilde{R}(\mathcal{M}^2\tilde{R}^2 - 1)^{-1/2}$ for $\tilde{R} \equiv R/R_p \geq 1$. Clearly, $\dot{R}_{\text{sh}} = c_s$ for $R/R_p \gg 1$, and $\dot{R}_{\text{sh}} = c_s\mathcal{M}/(\mathcal{M}^2 - 1)^{1/2}$ near $R/R_p = 1$ as equation (C1) implies. This prediction is roughly consistent with Escala et al. (2004) who empirically found that the tail in a model with $\mathcal{M} = \sqrt{2}$ has an average propagation speed of $\dot{R}_{\text{sh}} \approx 1.1c_s$.

Many previous studies on dynamical friction adopted the drag formula based on perturbers moving straight and estimated the Coulomb logarithm by taking $r_{\text{max}} = R_{\text{sys}}$, where R_{sys} is the system size (see references in §1). Unlike a straight-line trajectory, a circular orbit naturally introduces a characteristic length scale, R_p . The results of our semi-analytic analyses suggest that, at least in a gaseous medium, the drag force obtained for linear-

trajectory perturbers can be a reasonable approximation to that for circular-orbit perturbers with the same Mach number if $r_{\max} \equiv V_p t$ is taken equal to $2R_p$. Since $R_{\text{sys}} > 2R_p$ in most relevant situations, using $r_{\max} = R_{\text{sys}}$ usually overestimates the drag force for objects in near-circular motion. From hydrodynamic simulations for orbital decay of perturbers in a stratified gaseous sphere, Sánchez-Salcedo & Brandenburg (2001) suggested $\ln(\Lambda) = \ln(r_{\max}/r_{\min}) \rightarrow 2.34 \ln(0.79R_p/r_{\min})$ with an identification $r_{\min} = 2.25R_{\text{soft}}$, where R_{soft} is the softening radius of the point-mass potential (Sánchez-Salcedo & Brandenburg 1999). This happens to be similar to our suggestion $\ln(\Lambda) \rightarrow \ln(2R_p/r_{\min})$ for the parameter range $R_p/r_{\min} \sim 2 - 6$ that they considered.

Our suggestion for the Coulomb logarithm on near-circular orbit perturbers in a gaseous medium is also consistent with the common prescription for orbital decay of small satellites in collisionless backgrounds (e.g., Tremaine 1976; Lin & Tremaine 1983; Hashimoto et al. 2003; Fujii et al. 2006). In particular, Hashimoto et al. (2003) found that Chandrasekhar’s formula with $\ln(\Lambda) \rightarrow \ln[R_p/(1.4R_{\text{soft}})]$ gives excellent fits to the results of their N-body simulations. The discrepancy between our suggestion and their prescription may be attributable in part to the effects of collisionless nature, nonuniform background density, and self-gravity of particles in their models.

Density inhomogeneity in the background can also make significant changes to the classical drag force. For collisionless backgrounds, Just & Peñarrubia (2005) found that nonuniform density induces an additional drag force in the lateral direction of the perturber motion, taking up to 10% of the drag in the backward direction. They proposed the inverse of a local density gradient as an appropriate choice for r_{\max} in the Coulomb logarithm (see also Spinnato et al. 2003), which was confirmed by Arena & Bertin (2007) who ran a number of numerical simulations for systems with a large central density concentration. Hydrodynamic models in Sánchez-Salcedo & Brandenburg (2001) studied the combined effects of nonuniform backgrounds and curvilinear orbits on dynamical friction in a gaseous medium, although it is challenging to isolate each effect separately.

Finally, as a heuristic example, we consider the dynamical friction of a galaxy on a near-circular orbit subject to the drag force given by equations (13) and (14) due to an intracluster medium. The cluster is dominated by dark matter whose mass distribution follows the NFW profile with the characteristic mass $M_0 = 6.6 \times 10^{14} M_\odot$ and the scale radius $r_s = 460$ kpc (Navarro et al. 1996). The intracluster medium has a constant electron density $n_e = 0.05 \text{ cm}^{-3}$ and temperature 1 keV; the corresponding adiabatic speed of sound is $c_s = 500 \text{ km s}^{-1}$. Initially, a galaxy with size $r_{\min} = 10$ kpc and mass $M_p = 5 \times 10^{11} M_\odot$ including a dark halo (e.g., Zentner & Bullock 2003; Halkola et al. 2007) is orbiting at $R_0 = 100$ kpc with an equilibrium velocity $V_p = 10^3 \text{ km s}^{-1}$ about the cluster center. The equations

of motion in the orbital plane are

$$\ddot{R} - R\dot{\varphi}^2 = -(\mathcal{F}/M_p)\mathcal{I}_R - \frac{d\Phi_{\text{NFW}}}{dR}, \quad (15a)$$

$$R\ddot{\varphi} + 2\dot{R}\dot{\varphi} = -(\mathcal{F}/M_p)\mathcal{I}_\varphi, \quad (15b)$$

where Φ_{NFW} is the NFW potential and dots represent derivatives with respect to time. Figure 9 plots the resulting temporal variations of the orbital radius of the galaxy. The solid line corresponds to the case with full \mathcal{I}_R and \mathcal{I}_φ given by equations (13) and (14), while the dashed line is for a controlled case where \mathcal{I}_R is artificially taken to be zero. Except for slight mismatches in phase, both agree fairly well with each other, demonstrating that the radial drag force does not have a serious impact on the orbital decay. As equation (15) implies, it is the azimuthal drag \mathcal{I}_φ that takes away most of the orbital angular momentum from the galaxy; the radial drag changes the orbital eccentricity more than the semi-major axis (Burns 1976; see also Just & Peñarrubia 2005).

Figure 9 also plots as dot-dashed line the decay of the orbital radius blindly using Ostriker’s formula with $\ln(V_p t/r_{\min}) = 4.6$, corresponding to $V_p t = 1$ Mpc. While the galaxy motion remains supersonic ($t < 1.5$ Gyr), this value of the Coulomb logarithm overestimates the realistic drag force, on average, by a factor of 1.7 and thus brings the galaxy to $R = 0.1R_0$ in 2 Gyrs, which is about 2.3 times faster than the estimate based on the realistic drag force. On the other hand, the result of using $V_p t = 2R(t)$ in the formula of O99, shown as dotted line in Figure 9, is in excellent agreement with those using equations (13) and (14). This demonstrates again that Ostriker’s formula with $V_p t = 2R$ gives quite a good approximation to the drag force even in the case of a circular-orbit perturber.

We are grateful to E. Ostriker for suggesting this project and making stimulating comments. We also acknowledge a thoughtful report from the referee, A. Escala, and helpful comments from J. Sánchez-Salcedo. This work was supported by Korea Science and Engineering Foundation (KOSEF) grant R01-2004-000-10490-0 at SNU. H. Kim has been partially supported by the BK21 project of the Korean Government. The numerical computations presented in this work were performed on the Linux cluster at KASI (Korea Astronomy and Space Science Institute) built with funding from KASI and ARCSEC.

A. Solutions for $\mathcal{D}(\mathbf{x}, t)$ Near the Perturber

In this Appendix, we explore the approximate solutions to equation (8) near the perturber ($|\tilde{R}-1|, |s|, |\tilde{z}| \ll 1$). For subsonic motion ($\mathcal{M} < 1$), $|w_i| \ll 1$ and $d \approx (\delta^2 + w^2 + \tilde{z}^2)^{1/2}$

with $\delta \equiv \tilde{R} - 1$. In this case, equation (9) has a single root,

$$w_1 = \frac{s + \mathcal{M}[s^2 + (1 - \mathcal{M}^2)(\delta^2 + \tilde{z}^2)]^{1/2}}{\mathcal{M}^2 - 1}. \quad (\text{A1})$$

Inserting w_1 into equation (8) and retaining the first-order terms in $|\tilde{R} - 1|$, $|s|$, and $|\tilde{z}|$, one obtains $\mathcal{D}(\mathbf{x}) = [s^2 + (1 - \mathcal{M}^2)(\delta^2 + \tilde{z}^2)]^{-1/2}$ at a steady state, whose functional form is identical to equation (9) of O99 for $\mathcal{M} < 1$. Obviously, the equi-density surfaces of this distribution are oblate spheroids with the short axis parallel to the direction of the motion of the perturber.

For supersonic motion ($\mathcal{M} > 1$), we seek for asymptotic solutions of \mathcal{D} just behind the perturber along its orbit (i.e., $0 < -s \ll 1$, $\tilde{R} = 1$, $\tilde{z} = 0$). We further restrict the discussion to not-so-highly supersonic cases³, for which equation (9) has three roots:

$$w_1 \approx -\frac{s}{1 + \mathcal{M}}, \quad (\text{A2a})$$

$$w_2 \approx -\frac{s}{1 - \mathcal{M}}, \quad (\text{A2b})$$

$$w_3 \approx w_0 - s \left(1 - \frac{\mathcal{M}^2 \sin w_0}{w_0} \right)^{-1}, \quad (\text{A2c})$$

as long as $0 < -s \ll (\mathcal{M} - 1)^{3/2}$. Here, w_0 is a non-zero solution of

$$\mathcal{M}(2 - 2 \cos w_0)^{1/2} + w_0 = 0 \quad (\text{A3})$$

for given \mathcal{M} ($\neq 1$). Note that w_1 and w_2 are analogous to two solutions of O99 that contribute the wake in the rear Mach cone for a linear-trajectory perturber, while w_3 is a new solution introduced by a circular orbit. For $\mathcal{M} \rightarrow 1^{+0}$, $w_0 \rightarrow -[24(\mathcal{M} - 1)]^{1/2}$.

Substituting equations (A2) into equation (8) and taking the steady-state limit ($\mathcal{H} \rightarrow 1$), we obtain

$$\mathcal{D}(s) = \frac{2}{|s|} + \frac{\mathcal{M}}{\mathcal{M}^2 \sin w_0 - w_0}, \quad (\text{A4})$$

for $-s \ll (\mathcal{M} - 1)^{3/2}$. The first term in the right-hand side of equation (A4) again represents the perturbed density in the linear trajectory case. The second term, albeit small compared with the first term for small $|s|$, arises as the perturber on a circular orbit can overtake its wake. The effects of circular orbits are significant in regions away from the perturber, which is pursued numerically in §3.

³More precisely, $1 < \mathcal{M} < \mathcal{M}_1$, where \mathcal{M}_1 is a critical Mach number discussed in Appendix B.

B. Number of Roots for w_i of Equation (9)

To obtain the perturbed density $\mathcal{D}(\mathbf{x}, t)$ at given time and location, it is crucial to find w_i that satisfies equation (9). Let us define $f(w) \equiv \mathcal{M}d(w; \tilde{R}, \tilde{z})$ for a fixed set of $\mathcal{M}, \tilde{R}, \tilde{z}$, and s . Then, finding solutions of equation (9) is equivalent to finding the intersections of two curves $y = -w - s$ and $y = f(w)$ on the $w - y$ plane. Since $|df/dw| \leq \mathcal{M}$ for all \tilde{R} and \tilde{z} , it is trivial to show that there is only one solution for all space and time if $\mathcal{M} < 1$. This implies that any location inside the casual region for sound waves is influenced just once by a perturber moving at a subsonic speed. The same is true for a subsonic perturber moving on a straight-line trajectory studied by O99.

A necessary condition for having more than one root is $|df/dw| > 1$ for any w , which after some algebra results in

$$\mathcal{M} > 1, \quad \tilde{R} > \mathcal{M}^{-1}, \quad \text{and} \quad |\tilde{z}| < \mathcal{M}^{-1} (\mathcal{M}^2 - 1)^{1/2} (\mathcal{M}^2 \tilde{R}^2 - 1)^{1/2}. \quad (\text{B1})$$

When the conditions (B1) are fulfilled, there are two tangent points of the curve $y = f(w)$ to lines with a slope of -1 in the range $-\pi < w < 0$. Let (w_+, y_+) and (w_-, y_-) denote the tangent points, such that $-\pi < w_- < w_+ < 0$ and $0 < y_+ < y_- < \mathcal{M}$. The tangent condition $df/dw|_{w_{\pm}} = -1$ yields

$$w_{\pm} = -\cos^{-1} \left(\frac{1 \pm (\mathcal{M}^2 - 1)^{1/2} (\mathcal{M}^2 \tilde{R}^2 - 1)^{1/2}}{\mathcal{M}^2 \tilde{R}} \right), \quad (\text{B2a})$$

$$y_{\pm} = |(\mathcal{M}^2 \tilde{R}^2 - 1)^{1/2} \mp (\mathcal{M}^2 - 1)^{1/2}|, \quad (\text{B2b})$$

at the $z = 0$ plane. Note that the 2π periodicity of $y = f(w)$ ensures that $(w_{\pm} + 2\pi n, y_{\pm})$ for arbitrary integer n are also tangent points to a line with slope of -1 .

For given $\mathcal{M} > 1$, the number of solutions of equation (9) depends on the slopes of lines connecting the points $(w_- - 2\pi n, y_-)$ and (w_+, y_+) . When the line passing through $(w_- - 2\pi, y_-)$ and (w_+, y_+) has a slope larger than -1 , which occurs for $1 < \mathcal{M} < \mathcal{M}_1$ (see below for the definition of \mathcal{M}_n with integer $n \geq 1$), the spatial regions that satisfy equations (B1) as well as $w_+ + y_+ < -s < w_- + y_-$ have three roots for w_i , while the other regions have only a single root. When $\mathcal{M}_1 < \mathcal{M} < \mathcal{M}_2$, the slope of the line connecting $(w_- - 4\pi, y_-)$ and (w_+, y_+) is greater than -1 , so that the regions bounded by the condition $w_+ + y_+ < -s < w_- + y_- - 2\pi$ possess five roots; the other regions have three roots. Note that the volume that does not satisfy conditions (B1) still has a single root. As the Mach number increases further, new regions emerge to have a larger (odd) number of roots for w_i . Generalizing the discussion given above, the critical Mach number \mathcal{M}_n below which a steady-state wake possesses up to $2n + 1$ roots can be determined by the requirement

$(y_+ - y_-)/(w_+ - w_- + 2\pi n) = -1$. Using equations (B2), this is simplified to

$$2(\mathcal{M}_n^2 - 1)^{1/2} - \cos^{-1}(2\mathcal{M}_n^{-2} - 1) = 2\pi n, \quad (\text{B3})$$

where we take $\tilde{R} = 1$ without any loss of generality since the existence of multiple roots requires $\tilde{R} > \mathcal{M}^{-1}$ (eq. [B1]). The first few solutions of equation (B3) are $\mathcal{M}_1 = 4.6033$, $\mathcal{M}_2 = 7.7897$, $\mathcal{M}_3 = 10.9499$, etc.

The presence of multiple roots implies that the density wake in those regions are constructed by a superposition of sonic signals that were emitted by the perturber at as many different locations (and corresponding retarded times) as the number of roots. The \mathcal{M} -dependency of the number of roots for a circular-orbit supersonic perturber is in sharp contrast to the case of a straight-line trajectory where only one (within a sonic sphere) or two (within a rear Mach cone) roots are allowed regardless of the Mach number (O99). When a perturber is moving at a supersonic speed along a circular orbit, it is able to catch up with its own wake (possibly multiple times), adding new sonic disturbances to the regions that were already disturbed by the perturber. Regions of multiple roots usually take a form of a long trailing spiral, as exemplified in Figures 2, 3, and 4.

C. HALF-OPENING ANGLE

Although a Mach cone is generally curved for a circular-orbit perturber, its half-opening angle in the vicinity of the perturber is the same as in the linear trajectory counterpart. As explained in §3.1.1, the interior of a curved Mach cone and an attached trailing tail is the region where equation (9) has multiple roots in a steady state. It is bounded by $-s = w_{\pm} + y_{\pm}$ curves in the $z = 0$ plane. More specifically, the $-s = w_+ + y_+$ curve describes the inner and outer edges of the Mach cone head near the perturber as well as the outer edge of the tail, represented by light solid curve and dashed curve at the boundaries of the shade region displayed in Figure 1. On the other hand, the $-s = w_- + y_-$ curve corresponds to the inner edge of the tail (dot-dashed curve in Fig. 1) that meets the Mach cone head at $\tilde{R} = \mathcal{M}^{-1}$. By Taylor expanding w_+ and y_+ about $\tilde{R} = 1, s = 0$ in the $z = 0$ plane and adding the resulting expressions together, one can show the head of the Mach cone is described by

$$s = -(\mathcal{M}^2 - 1)^{1/2}|\delta|, \quad (\text{C1})$$

up to the first order in $|\delta| \equiv |\tilde{R} - 1|$. The negative sign in equation (C1) results since s is measured in the counterclockwise direction from the perturber (Fig. 1). Let θ be the half-opening angle of the Mach cone near the perturber. Then, $\tan \theta = -|\delta|/s = (\mathcal{M}^2 - 1)^{-1/2}$, or $\theta = \sin^{-1}(1/\mathcal{M})$, the same result as in the linear trajectory case.

REFERENCES

- Arena, S. E., & Bertin, G. 2007, *A&A*, 463, 921
- Binney, J., & Tremaine, S. 1987, *Galactic Dynamics* (Princeton: Princeton Univ. Press)
- Bullock, J. S., Johnston, K. V. 2005, *ApJ*, 635, 931
- Burns, J. A. 1976, *American Journal of Phys.*, 44, 944
- Chandrasekhar, S. 1943, *ApJ*, 97, 255
- Chang, H.-Y. 2001, *ApJ*, 551, L159
- Chang, H.-Y., Choi, C.-S. 2003, *A&A*, 410, 519
- Del Popolo, A., Yeşilyurt, S., & Ercan, E. N. 2003, *MNRAS*, 339, 556
- Dokuchaev, V. P. 1964, *Soviet Astron.*, 8, 23
- Dotti, M., Colpi, M., & Haardt, F. 2006, *MNRAS*, 367, 103
- El-Zant, A. A., Kim, W.-T., & Kamionkowski, M. 2004, *MNRAS*, 354, 169
- Escala, A., Larson, R. B., Coppi, P. S., & Mardones, D. 2004, *ApJ*, 607, 765
- Escala, A., Larson, R. B., Coppi, P. S., & Mardones, D. 2005, *ApJ*, 630, 152
- Faltenbacher, A., Kravtsov, A. V., Nagai, D., & Gottloeber, S. 2005, *MNRAS*, 358, 139
- Fujii, M., Funato, Y., & Makino, J. 2006, *PASJ*, 58, 743
- Furlanetto, S. R., & Loeb, A. 2002, *ApJ*, 565, 854
- Goldreich, P., Lithwick, Y., & Sari, R. 2002, *Nature*, 420, 643
- Halkola, A., Seitz, S., & Pannella, M. 2007, *ApJ*, 656, 739
- Hashimoto, Y., Funato, Y., & Makino, J. 2003, *ApJ*, 582, 196
- Hernquist, L., & Weinberg, M. D. 1989, *MNRAS*, 238, 407
- Jackson, J. D. 1975, *Classical Electrodynamics* (New York: Wiley)
- Just, A., & Peñarrubia, J. 2005, *A&A*, 431, 861
- Karas, V., Šubr, L. 2001, *A&A*, 376, 686

- Kim, S. S., & Morris, M. 2003, ApJ, 597, 312
- Kim, S. S., Figer, D. F., & Morris, M. 2004, ApJ, 607, L123
- Kim, W.-T., El-Zant, A. A., & Kamionkowski, M. 2005, ApJ, 632, 157
- Lin, D. N. C., Tremaine, S. 1983, ApJ, 264, 364
- Liu, F. K. 2004, MNRAS, 347, 1357
- McMillan, S. L. W., Portegies Zwart, S. F. 2003, ApJ, 596, 314
- Mulder, W. A. 1983, A&A, 117, 9
- Narayan, R. 2000, ApJ, 536, 663
- Navarro, J. F., Frenk, C. S., & White, S. D. M. 1996, ApJ, 462, 563
- Ostriker, E. C. 1999, ApJ, 513, 252 (O99)
- Rephaeli, Y., & Salpeter, E. E. 1980, ApJ, 240, 20
- Ruderman, M. A., & Spiegel, E. A. 1971, ApJ, 165, 1
- Sánchez-Salcedo, F. J., & Brandenburg, A. 1999, ApJ, 522, L35
- Sánchez-Salcedo, F. J., & Brandenburg, A. 2001, MNRAS, 322, 67
- Spinnato, P. F., Fellhauer, M., Portegies Z., & Simon F. MNRAS, 344, 22
- Tremaine, S. D. 1976, ApJ, 203, 72
- Weinberg, M. D. 1989, MNRAS, 239, 549
- Zentner, A., & Bullock, J. S. 2003, ApJ, 598, 49

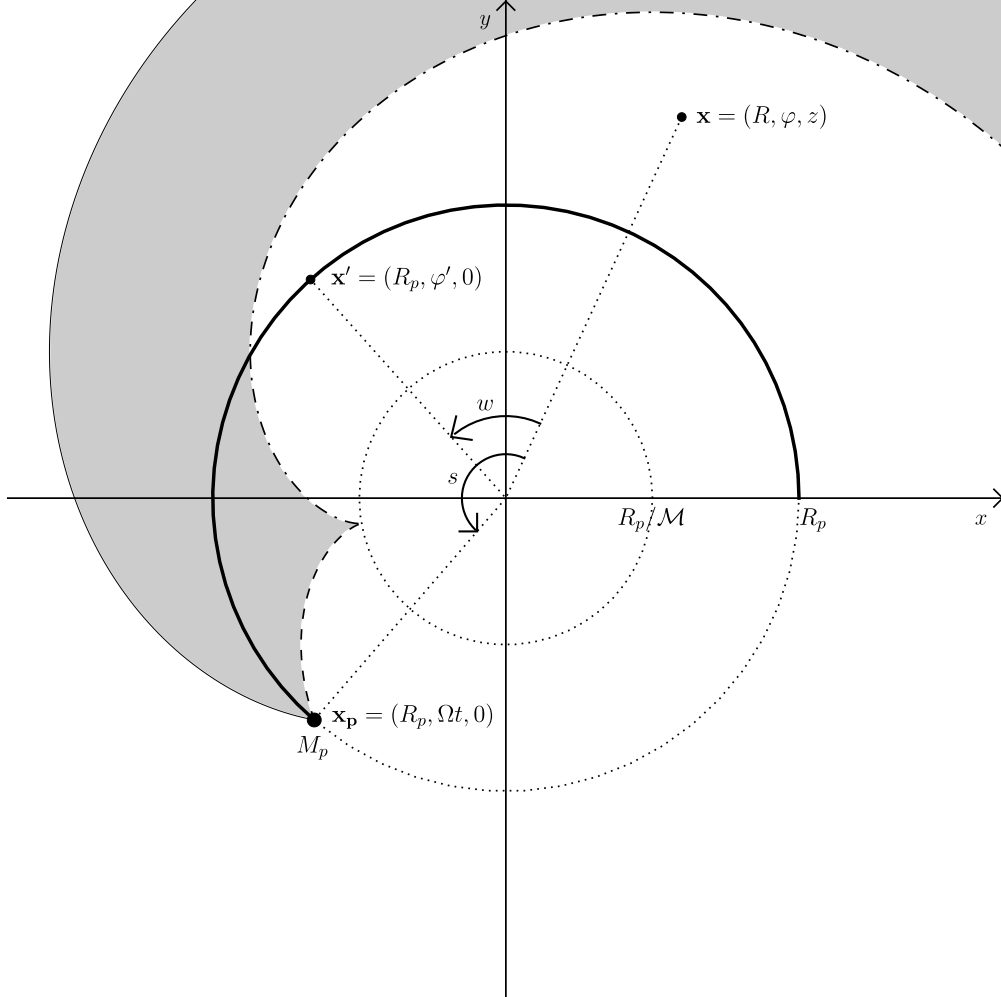


Fig. 1.— Schematic diagram illustrating the situation on the $z = 0$ plane at time t . A perturber initially introduced at $(R_p, 0, 0)$ moves along a circle with radius R_p at uniform angular speed Ω in the counterclockwise direction, and is currently at the position $\mathbf{x}_p \equiv (R_p, \Omega t, 0)$. At this time, an observer sitting at $\mathbf{x} = (R, \varphi, z)$ receives a sonic signal that was emitted by the perturber when it was at $\mathbf{x}' = (R_p, \Omega t', 0)$, where $t' = t - |\mathbf{x} - \mathbf{x}'|/c_s$ is the retarded time. The angular variables are $w \equiv \varphi' - \varphi$ and $s \equiv \varphi - \Omega t$ along the orbital plane. The shaded area represents a curved Mach cone and a wake tail formed by a supersonic perturber with $\mathcal{M} > 1$. The inner edge (dashed curve) of the Mach cone meets the inner edge (dot-dashed curve) of the tail at a point on a circle with radius R_p/\mathcal{M} . The outer edge (light solid curve) of the Mach cone defines the outer edge of the tail.

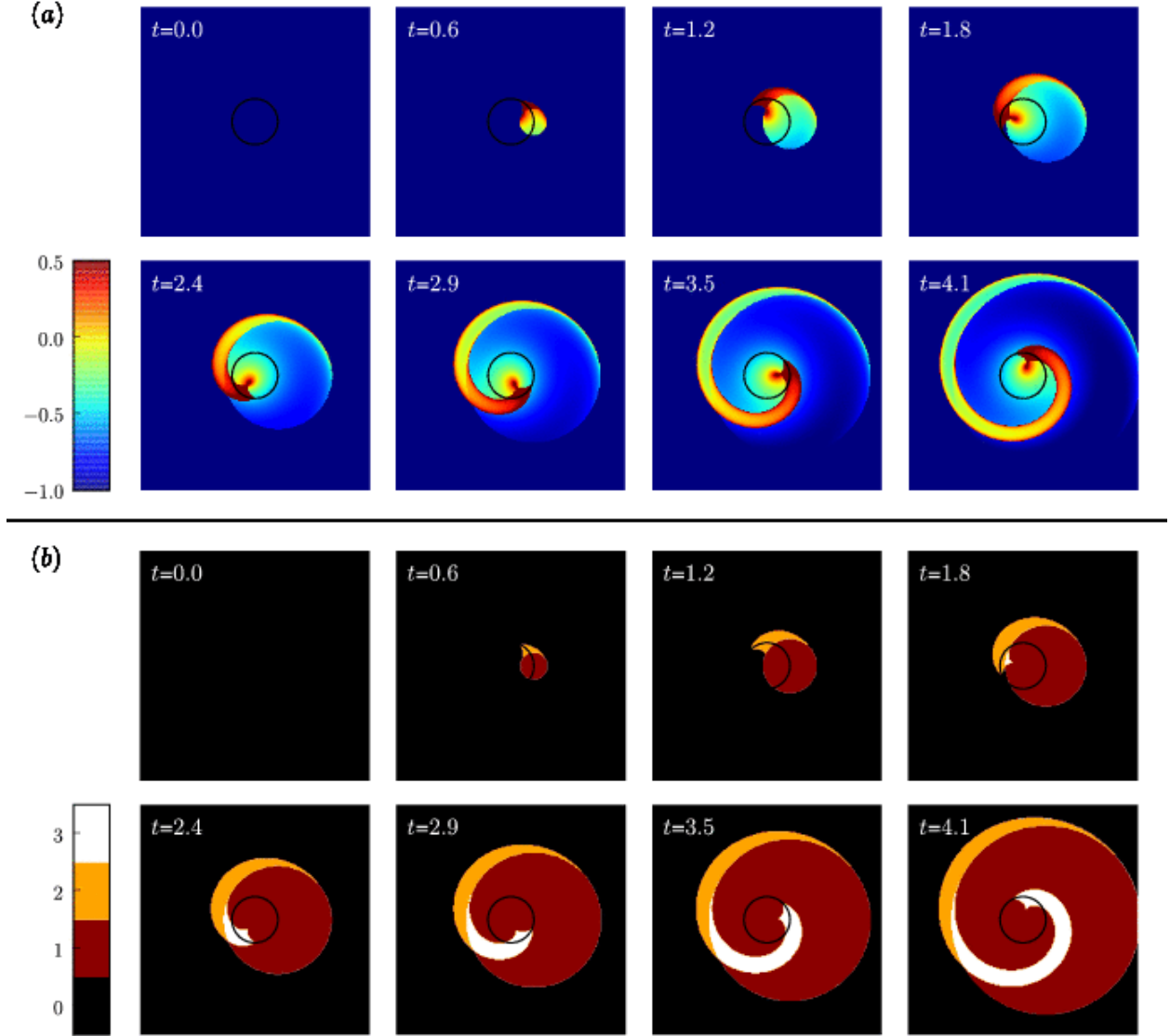


Fig. 2.— Temporal evolution at the $z = 0$ plane of (a) the dimensionless density wake $\mathcal{D}(\mathbf{x}, t)$ in logarithmic color scale and (b) the number of roots for w_i in equation (9) for the case of $\mathcal{M} = 2.0$. The time is in unit of R_p/c_s . See text for details.

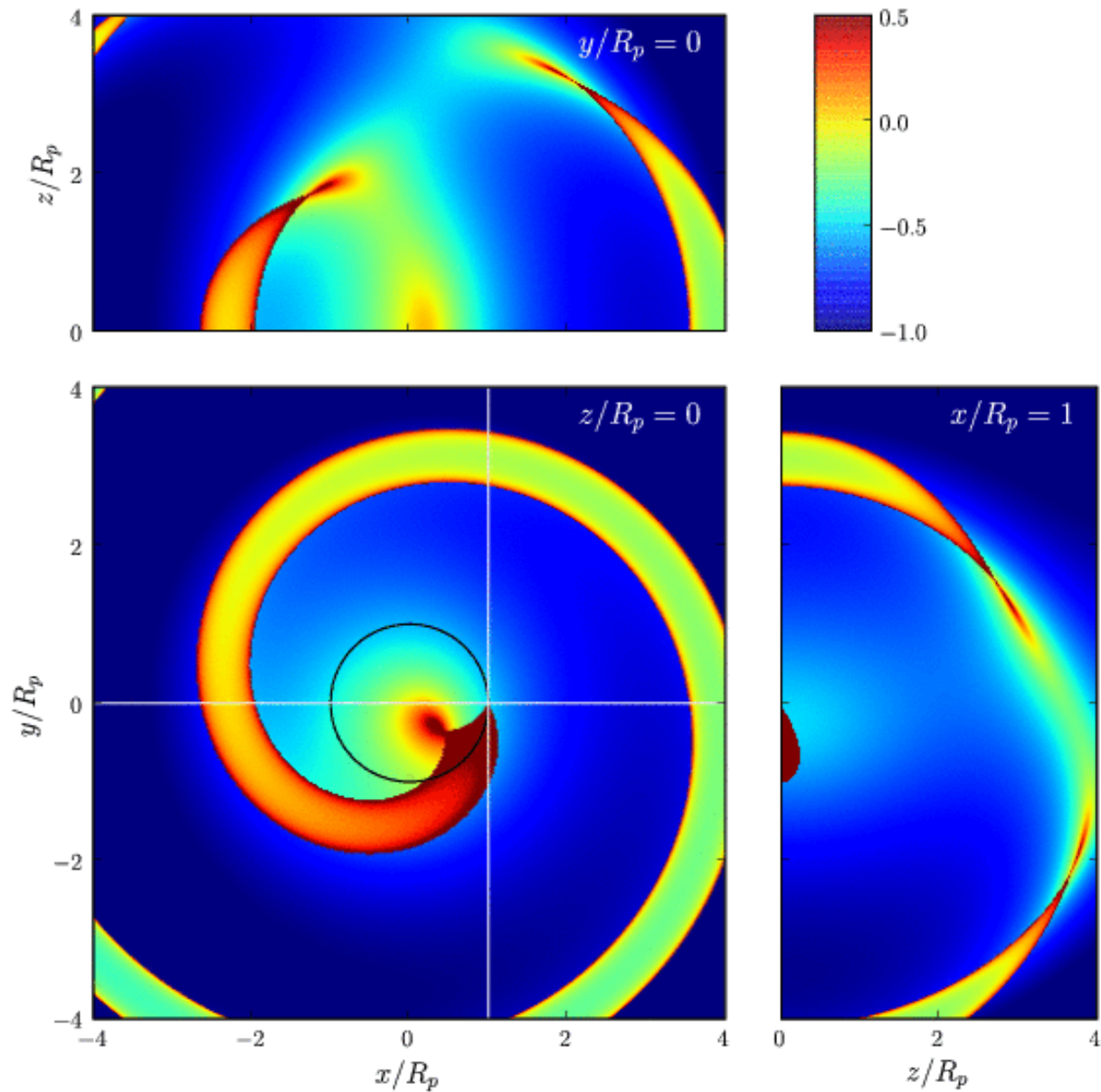


Fig. 3.— Density distributions of the steady-state wake for $\mathcal{M} = 2.0$ on the $x/R_p = 1$ (bottom right), $y = 0$ (top left), and $z = 0$ (bottom left) planes. The perturber is located at $(x, y) = (R_p, 0)$, and the black circle in the bottom left frame denotes the orbit of the perturber. Color bar labels $\log \mathcal{D}$.

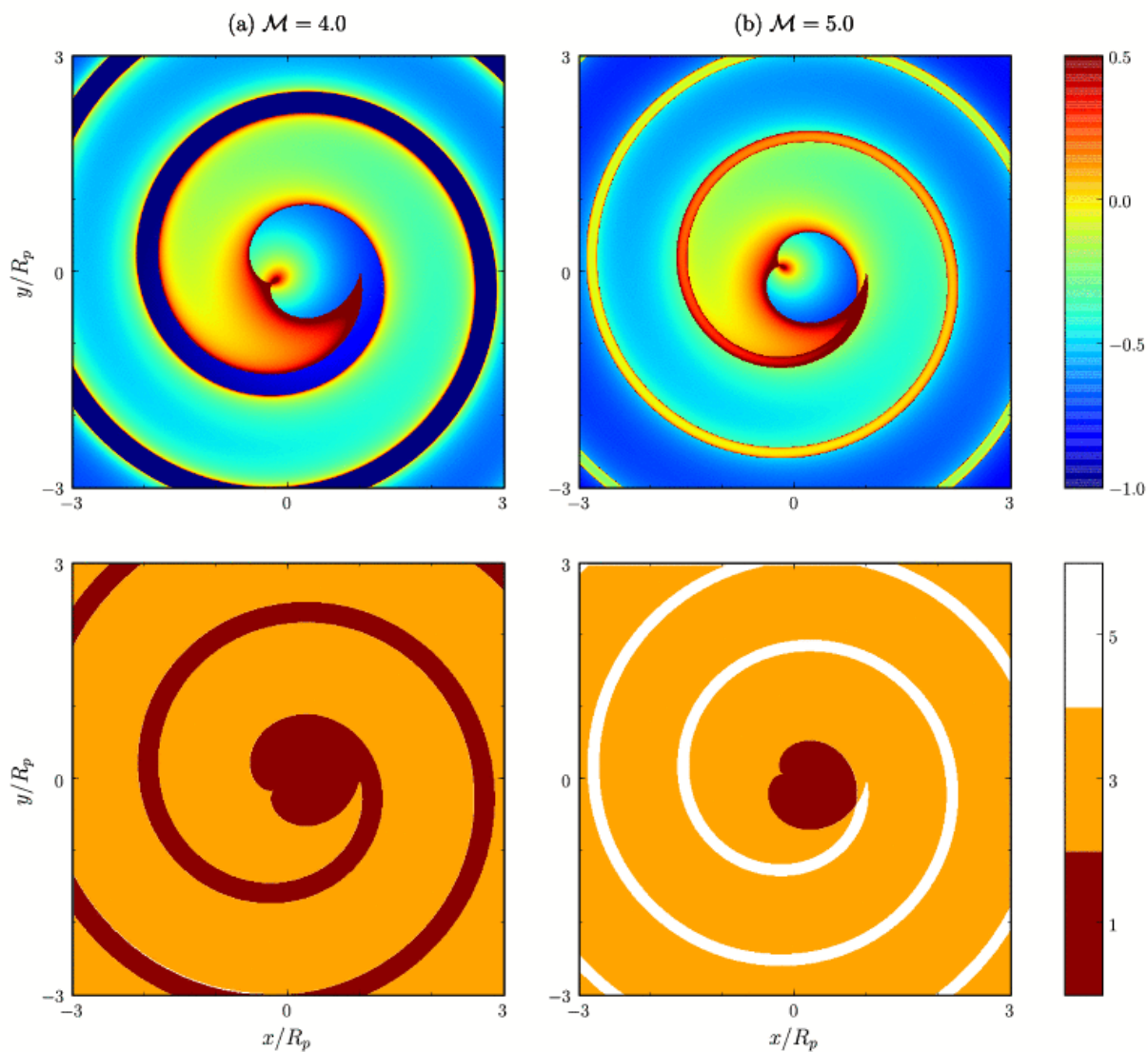


Fig. 4.— Distributions of the perturbed density \mathcal{D} in logarithmic color scale (*top*) and the corresponding number of roots for w_i in equation (9) (*bottom*) at the $z = 0$ plane of the steady-state wake for (a) $\mathcal{M} = 4.0$ and (b) $\mathcal{M} = 5.0$. The perturber is located at $(x, y) = (R_p, 0)$.

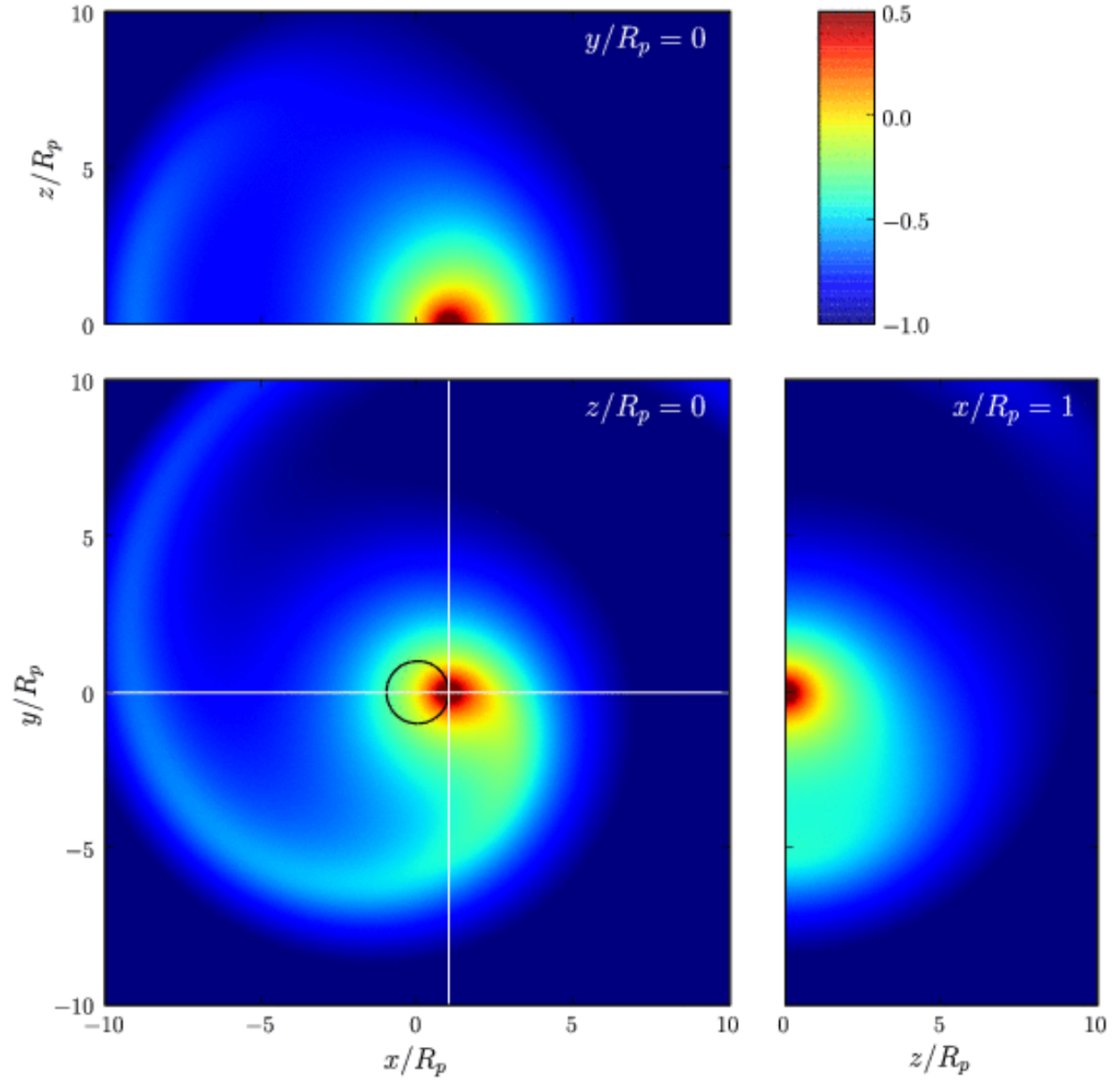


Fig. 5.— Same as Fig. 3 except for $\mathcal{M} = 0.5$.

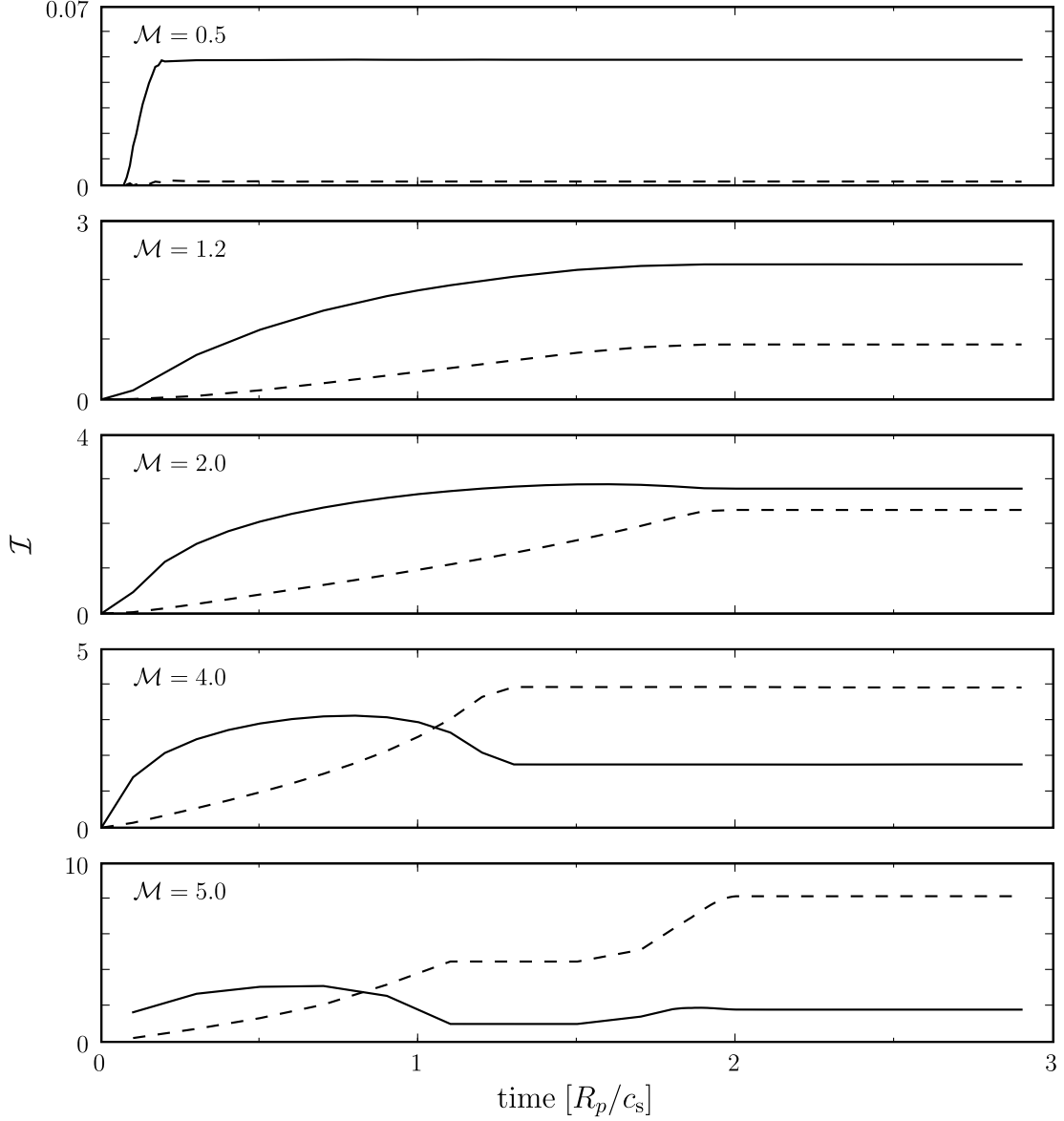


Fig. 6.— Time evolution of the drag force for $\mathcal{M} = 0.5, 1.2, 2.0, 4.0,$ and 5.0 . Solid curves draw the azimuthal drag \mathcal{I}_φ , while dashed curves are for the radial drag \mathcal{I}_R . For all cases, $r_{\min} = R_p/10$ is taken. Note that both \mathcal{I}_φ and \mathcal{I}_R converge typically within the sound crossing time across $2R_p$, indicating that a steady state is reached quite rapidly.

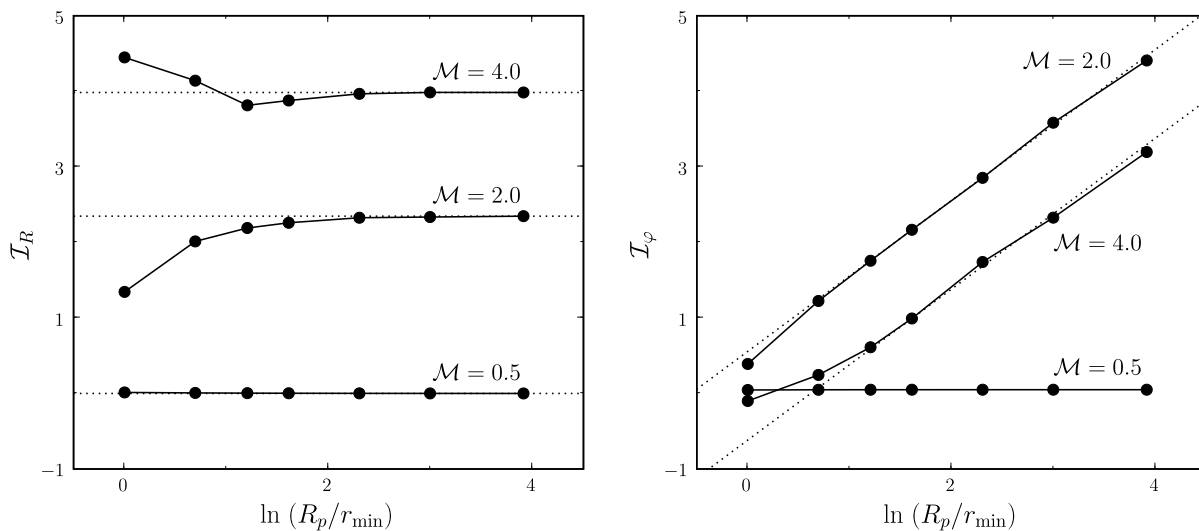


Fig. 7.— Dependence on r_{\min} of the steady-state drag force for $\mathcal{M} = 0.5, 2.0$, and 4.0 . *Left:* For $R_p/r_{\min} > 10$, the radial drag force \mathcal{I}_R converges to a respective constant value marked by dotted line. *Right:* The azimuthal drag force \mathcal{I}_φ varies as $\ln(R_p/r_{\min})$ for small r_{\min} when $\mathcal{M} > 1$, while independent of r_{\min} for $\mathcal{M} < 1$. Dotted lines indicate a slope of unity.

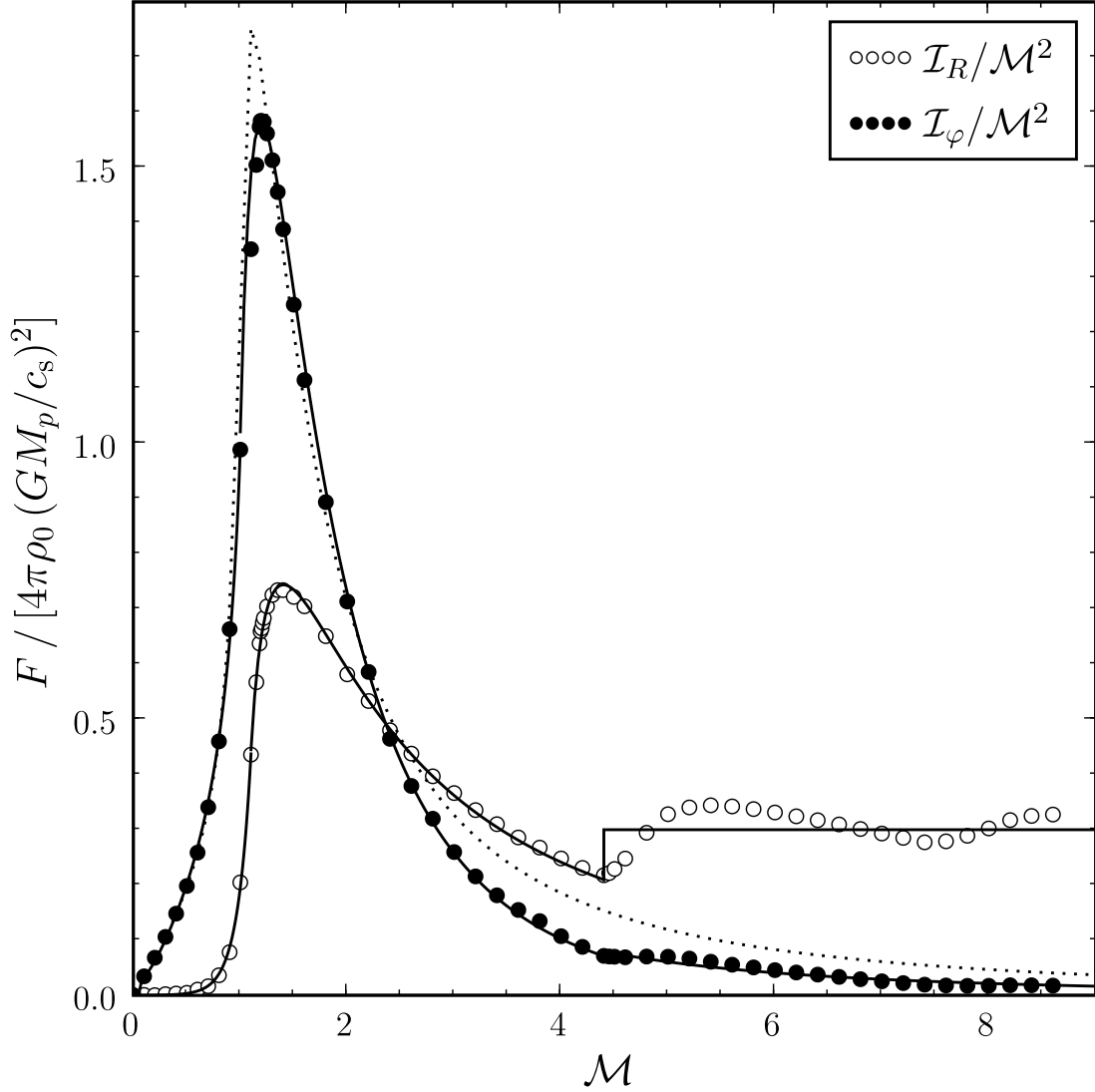


Fig. 8.— Gravitational drag force on a circular-orbit perturber in a gaseous medium as a function of the Mach number \mathcal{M} . The open and filled circles give the results of our semi-analytic calculation for the drag in the radial and azimuthal directions, respectively. For all the points, $r_{\min}/R_p = 0.1$ is taken. Solid lines draw the fits, equations (13) and (14), to the semi-analytic results. Dotted line corresponding to the force formula with $V_{pt} = 2R_p$ in O99 for the case of linear-trajectory perturbers is in quite a good agreement with the azimuthal drag for circular-orbit perturbers.

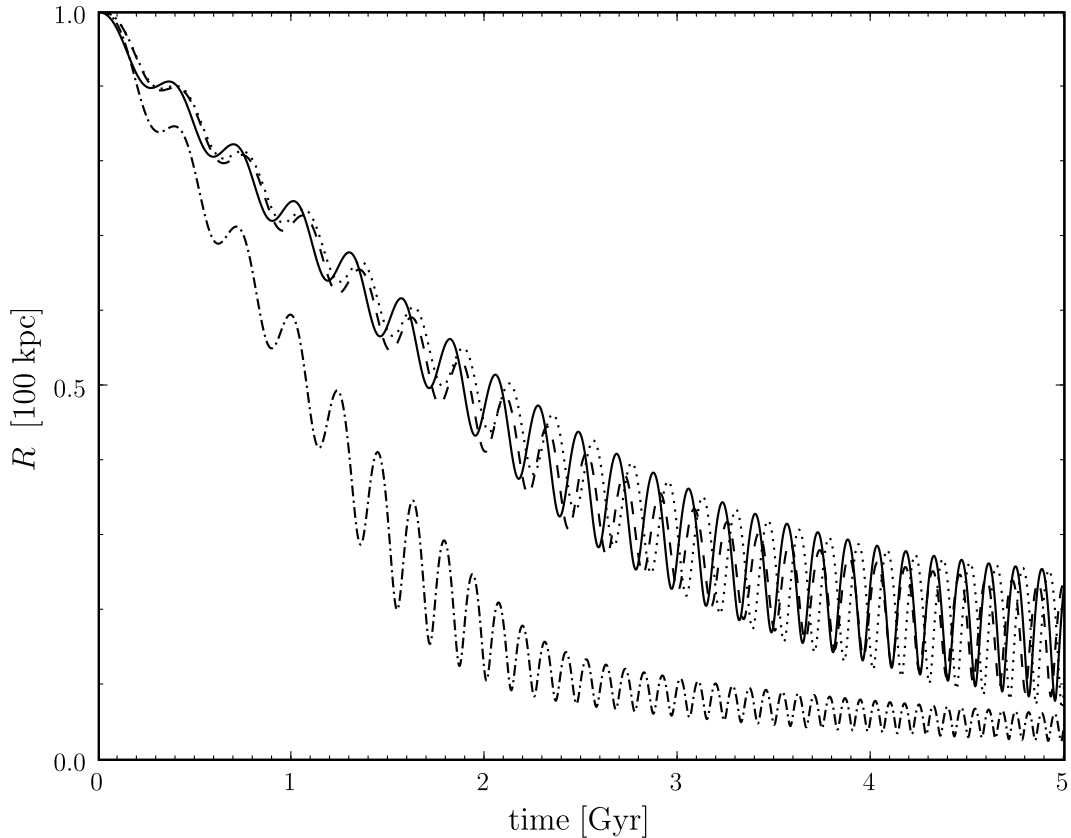


Fig. 9.— Orbital decay of a model galaxy caused by dynamical friction due to an intracluster gas. Solid line corresponds to the case when both \mathcal{I}_R (eq. [13]) and \mathcal{I}_φ (eq. [14]) are considered, while dashed line shows the result with only \mathcal{I}_φ (i.e., with $\mathcal{I}_R = 0$). For comparison, the results of Ostriker’s formula with fixed $V_p t = 1$ Mpc and varying $V_p t = 2R(t)$ are plotted as dot-dashed and dotted lines, respectively.